remote sensing

Article

Deformation Monitoring and Analysis of the Geological Environment of Pudong International Airport with Persistent Scatterer SAR Interferometry

Yanan Jiang [1,2,5], Mingsheng Liao [2,3,*], Hanmei Wang [4], Lu Zhang [2,3] and Timo Balz [2]

1 State Key Laboratory of Geohazard Prevention and Geoenviroment Protection, Chengdu University of Technology, Chengdu 610059, China; jiangyanan@cdut.edu.cn
2 State Key Laboratory of Information Engineering in Surveying, Mapping and Remote Sensing, Wuhan University, Wuhan 430079, China; luzhang@whu.edu.cn (L.Z.); balz@whu.edu.cn (T.B.)
3 Collaborative Innovation Center for Geospatial Technology, Wuhan 430079, China
4 Key Laboratory of Land Subsidence Monitoring and Prevention, Ministry of Land and Resources, Shanghai 200072, China; whm76@sigs.com.cn
5 College of Earth Sciences, Chengdu University of Technology, Chengdu 610059, China
* Correspondence: liao@whu.edu.cn; Tel.: +86-276-877-8070; Fax: +86-276-877-8229

Academic Editors: Qihao Weng, Guangxing Wang, George Xian, Hua Liu, Zhong Lu, Xiaofeng Li and Prasad S. Thenkabail
Received: 13 October 2016; Accepted: 8 December 2016; Published: 14 December 2016

Abstract: Many coastal cities have undertaken reclamation projects to satisfy the land demands of rapid urbanization. However, the foundations of reclaimed land are susceptible to settlement and can have undesirable environmental impacts that could adversely affect these dense, populated areas. In the case of international airports built on reclaimed areas especially, regional-scale deformation must be monitored to ensure operational security for public safety. Persistent Scatterer SAR Interferometry (PSI) technology has proven to be an effective tool to detect ground deformation in urban areas. However, it is still a challenge to apply PSI to effectively monitor settlement at airports built on newly developed coastal reclamation areas because of the scarcity of identifiable targets. Moreover, additional issues arise as the complicated deformation patterns associated with the underlying geological conditions make it difficult to interpret InSAR-derived results. In this study, a time-series analysis of a high-resolution TerraSAR-X satellite image stack acquired from September 2011 to October 2012 was performed by employing a modified PSI technique to retrieve the mean deformation velocity and time series of surface deformation at Pudong International Airport. Qualitative evaluation of spatial distribution and temporal evolution of deformation was conducted by joint analyses of deformation measurements and local geological data. Detailed analysis of various driving forces for deformation patterns confirmed that the results of deformation monitoring obtained by PSI are reliable and consistent with that of local geological surveys. Since the factors responsible for the subsidence within the airport are still at play, ongoing and routine deformation monitoring is warranted.

Keywords: deformation; geological environment; Shanghai Pudong International Airport; TerraSAR-X satellite images

1. Introduction

Given the fast pace of economic development, many seaside cities are experiencing a shortage of land for urban construction and transportation. To meet this growing need, it is a common practice to reclaim land from the sea in many coastal countries worldwide [1–4]. Over the past decades, many new airports servicing coastal cities have been built further away from populated areas and closer to the sea to mitigate the pressure on air transport, responding to varied land-use demands [1,5,6]. Hong Kong, Macao, Shanghai, Dalian and other cities have all reclaimed land from the sea for airport extensions. The Shanghai Pudong International Airport is one of these reclamation projects. Since an area reclaimed and used for construction has only a short history as land, it has a weak basic geology with little stability. Subsequently, for airports constructed on such areas, foundation settlement is a significant environmental geological problem [3,7]. Especially threatening is non-uniform settlement with serious safety implications, causing cracking or caving in buildings and infrastructure. Thus, the identification and monitoring of existing or potential deformation at airports is of vital importance when assessing risks. Understanding subsidence mechanisms is essential so that appropriate mitigation actions can be taken to prevent further damage.

Conventional methods to monitor deformation including layerwise mark, spirit leveling, and Global Position System (GPS), are based on point-by-point observations, and are labor-intensive and time consuming [8], especially for large linear facilities like roads and bridges that stretch for hundreds of thousands of kilometers. It is impractical to install sensors all along these structures, and thus, observations are limited in spatial coverage and density. As compared with traditional, ground-based geodetic deformation monitoring methods using sparse points, the InSAR technique can potentially provide a higher spatial resolution and sub-centimeter precision surface deformation measurements at a large scale. The technique uses two SAR images covering the same extent at different times and measures the phase difference between the two time periods to retrieve ground-surface displacement along the satellite line-of-sight (LOS) direction [9–15].

Since the InSAR technique was first introduced to study earthquakes by Massonnet et al., [16], a number of innovations have been made for overcoming limitations of temporal and spatial decorrelations as well as the atmospheric phase screen. These improvements have extended the application of the InSAR technique making them applicable to time-series subsidence monitoring. Among these innovations, the Persistent Scatterer SAR Interferometry (PSI) technique, first proposed by [17] was further developed to monitor the temporal evolution of deformation on each Permanent Scatterer (PS) to produce a deformation rate map at the millimeter level by processing time series SAR images [8,18–24]. These techniques have been proven to be an efficient method for investigating the spatial and temporal pattern of surface deformation [20,25–28].

A few studies have shown the capacity of the InSAR techniques to detect ground deformation phenomena in urban or suburban areas of Shanghai [29–32]. Nevertheless, it is still a challenge to monitor the settlement of Pudong International Airport built on newly developed coastal reclamation areas. First, radar echo signals from the runways decrease substantially due to the flat runway structure; whilst the similarity between the echo signals are low (so called low-coherence) as lawns are planted in the transitional zones of runways. This results in a scarcity of identifiable targets, which adversely affects the accuracy of deformation results. Moreover, the complicated deformation patterns; associated with the underlying geological conditions and building foundation types, in addition to ongoing construction activities, make it difficult to interpret InSAR-derived results. Especially, when moderately high spatial and temporal resolution SAR data, such as the ERS-1/2 and ENVISAT ASAR images are used, a sparse distribution of stable points are generated due to the limitations stemming from both the image resolution and the traditional method itself [33,34], making it unsuitable for representation of the spatial distribution of deformation over the airport runways and taxiways.

In our study, we focused on Shanghai Pudong International Airport, performed a time-series analysis of a high-resolution TerraSAR-X satellite image stack by employing a modified PSI technique. We aim to: (1) show the extent and spatiotemporal behavior of deformation in Shanghai Pudong International Airport, including the runways and taxiways; (2) combine the InSAR results with local geological data and reclamation evolution information available; and (3) make a time series analysis of various areas to reflect the deformation characteristics and analyze the driving force. Subsequently, a detailed analysis of the relationship between the observed subsidence and the driving force were carried out, concentrating especially on non-uniform settlement of the infrastructure and on the adjacent ground.

2. Description of the Study Area and SAR Dataset

2.1. Study Area

Shanghai Pudong International Airport is a major aviation hub for Asia. More than 51.6 million passengers and 3.18 million tons of cargo traveled through Shanghai Pudong International Airport in 2014. The airport started operations in 1999; phase two construction including a second terminal, a third runway, and a cargo terminal began in 2004. The Airport has two main passenger terminals, flanked on both sides by three parallel runways. However, only two terminals and three runways were in use before 2015, as can be seen in Figure 1.

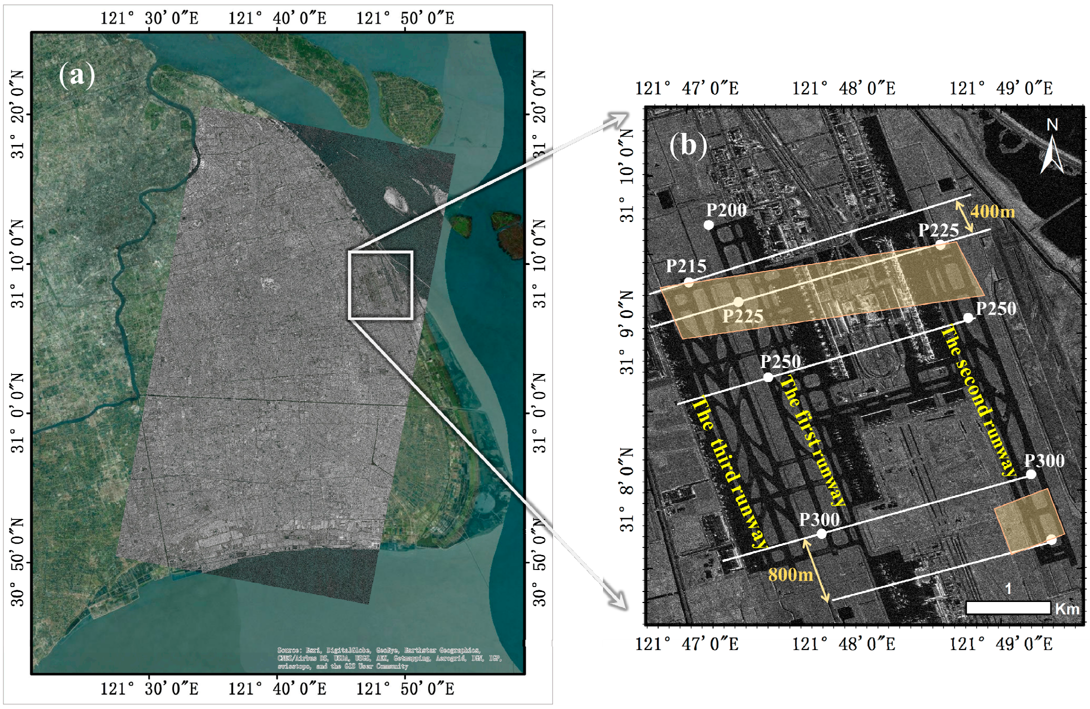

Figure 1. Area coverage of TerraSAR-X image (**a**) and the region of the paleo-river in mileage coordinates buried under the three runways (**b**).

The airport was built on an area of 40 km^2 on old and recently reclaimed land formed by both artificial fill materials and natural sediments. It is located on the southern bank of the Yangtze River estuary in the Pudong coastal zone, neighboring the East Sea. The first runway, located in the western half of the airport, is part of the first construction phase and has been in use since 1999. The second and third runways are located in a part of the second phase expansion project. The second runway has been in operation since 2005 and lies upon reclaimed land in the eastern part of the airport, while the third runway; in use since 2008, lies to the west of the first runway, and parallel to it. The future fourth and fifth runways will be located to the east of the second runway, near the East Sea.

The Pudong area is a type of coastal plain landform with a relatively flat terrain that was gradually built up by deposition over hundreds of years [35]. Similar to other reclaimed coastal areas, the reclaimed coastal geological environment is unstable. Moreover, the landform in Pudong International Airport contains a number of buried crisscrossed ditches and creek cuttings, leading to the falling of the soil strength with a non-uniform distribution [3]. Thus, many environmental geological problems are prone to arise during engineering and construction processes [36]. In particular, runways and other infrastructure here were constructed and founded on different foundation types during different reclamation periods. Therefore, complicated deformation patterns, associated with the underlying geological conditions and foundation types, might be observed by InSAR technology. Furthermore, the expansion of the fourth and fifth runways and other airport facilities was still underway during this study period. These construction activities and the complicated deformation patterns increase the difficulty of InSAR deformation monitoring and interpretation of the reclaimed land.

2.2. Dataset and Data Pre-Processing

As shown in Table 1, we applied interferometric processes to a descending dataset of 15 TerraSAR-X satellite images at VV polarization, acquired from September 2011 to October 2012 in StripMap mode. The resolution of the SAR images is about 3 m. Due to the high resolution of the images, airport runways and taxiways are clearly visible on the amplitude image (Figure 1). Considering the overall correlation coefficient [21], we selected the image acquired on 2 December 2011 as the master image. Then, interference processing between the master image and other co-registered images were implemented using an InSAR software named Doppler Orbitography and Radio-positioning Integrated by Satellite (DORIS). During this process, the Shuttle Radar Topography Mission (SRTM) 90 m digital elevation data [37] was used to simulate and remove the topographic phase and also for geocoding the InSAR results from range-Doppler coordinates into the WGS84 coordinate system. Basic information including temporal and perpendicular baselines of slave images with respect to the master image are shown in Table 1. As can be seen, the baselines are quite small, and conducive to follow-up processing, as large baselines cause decorrelations, and effect the measurements adversely [17].

Table 1. Basic parameters of TerraSAR images.

No.	Acquisition Date	Orbit	Time Baseline (Days)	Perpendicular Baseline (m)
1	27 September 2011	23,772	−66	−26
2	19 October 2011	24,106	−44	22
3	10 November 2011	24,440	−22	−41
4	**2 December 2011**	**24,774**	**0**	**0**
5	24 December 2011	25,108	22	157
6	26 January 2012	25,609	55	−60
7	28 February 2012	26,110	88	−159
8	21 March 2012	26,444	110	117
9	12 April 2012	26,778	132	119
10	26 May 2012	27,446	176	102
11	9 July 2012	28,114	220	−31
12	31 July 2012	28,448	242	50
13	13 September 2012	29,116	286	−71
14	24 September 2012	29,283	297	38
15	16 October 2012	29,617	319	59

3. Methodology

3.1. The PSI Technology

The PSI technique is an extension to the conventional InSAR technique that addresses decorrelation problems inherent in conventional InSAR techniques. It was first developed by [17] and later extended by many researchers [8,18–24]. The PSI technique makes use of a large set of SAR image pairs to produce many interferograms. Image pixels with strong scattering characteristics and stable phase information over long time periods (so called Permanent Scatterer (PS)) are selected and analyzed to produce the temporal evolution of deformation on each PS and then to provide a deformation rate map at a millimeter level. A detailed discussion on the PSI method is outside the scope of this work and can be found in [17,25]. In this study, we will focus on the key aspects of this method that make it suitable for airport deformation monitoring, including: the extraction of PS in low-coherence areas; the realization of phase analysis in time series; and the ability to deliver deformation for different periods. The process flow of the proposed PSI method is illustrated in Figure 2.

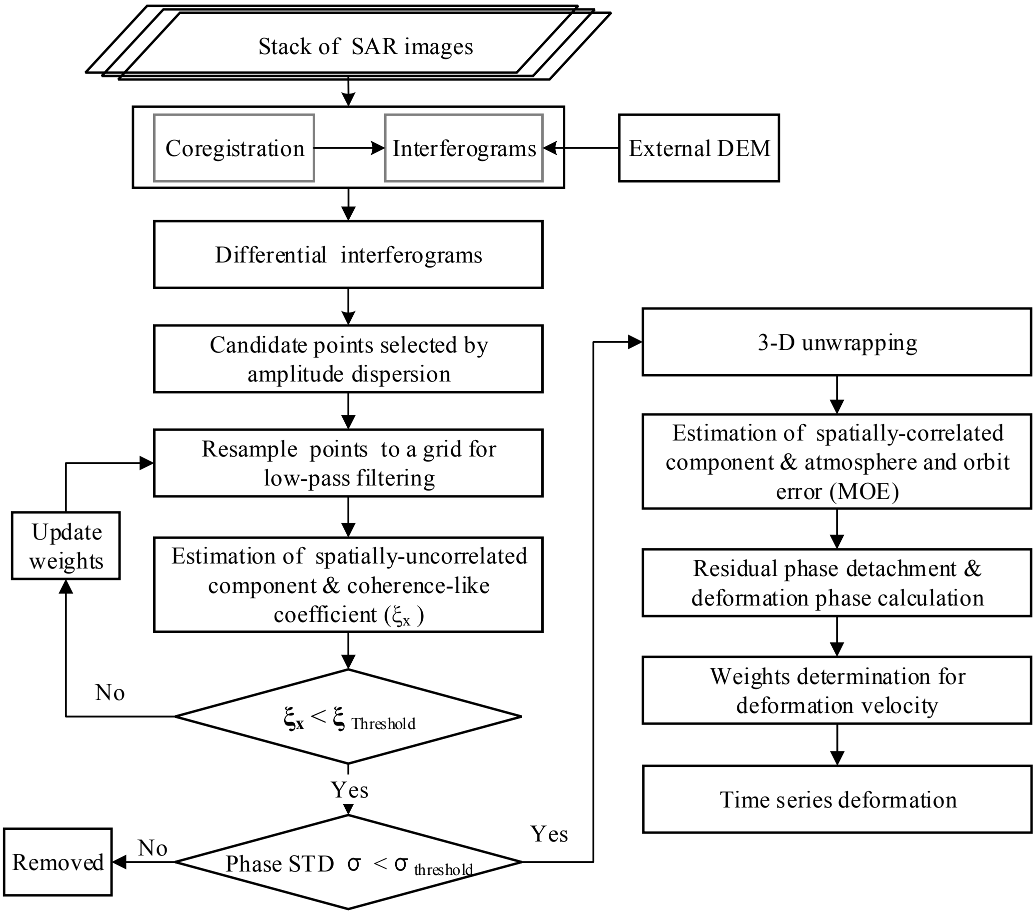

Figure 2. Flow chart of the proposed PSI technique.

3.2. Point Target Extraction in a Low-Coherence Area

In the traditional PSI technique, Amplitude Dispersion Index (ADI) is adopted to detect possible PS point. The ADI is defined as the ration of the standard deviation of the amplitude over its mean for a certain pixel [17,21,25]. However, the ADI based on the amplitude stability of individual pixels, is suitable for identifying PS points in areas with dense artificial features.

Runways of airports, however, are different from the other kinds of artificial features typically the subject of InSAR analysis. Unlike road networks, InSAR runway data shows low-coherence because of the lawns planted in the runway and taxiways transitional zones; especially when an airport is built on reclaimed coastal land. Only a limited number of PS can be identified, which adversely affects the accuracy of deformation results. One response is to enlarge the threshold value of the ADI to account for these differences but the probability of error will increase. Thus, another method should be incorporated to settle the problem of the increased error.

The coherence-like coefficient method can obtain a higher density of points than the ADI in low-coherence areas [23,38]. This method uses the phase stability of each pixel to separate the disturbance term from the interferometric phase to extract PS points. However, because of the filtering operation, it reduces, to some degree, the resolution of the image and generates false targets during point selection [38].

Considering the statistical relationship between the amplitude stability and phase stability, a point selection strategy that unites the ADI with the coherence-like coefficient is applied in our study to select point targets in low-coherence areas. Our method is as follows:

1. Initial pixel candidates are selected based on the amplitude stability of individual pixels, using a higher amplitude dispersion threshold value (0.4).
2. Preliminary elimination of pixel candidates is then carried out based on the phase stability of the pixels. High coherence PS candidates are chosen by iteration using the coherence-like coefficient method [20].
3. A standard deviation (STD) threshold for the phase is set for PS candidates to exclude pseudo PS points; in the case of Pudong International Airport, points with phase STDs larger than the indicated threshold value (>0.7) were considered as unstable points and rejected.

3.3. Phase Analysis and Deformation Calculation

After PS point recognition, the observed phase of i-th PS point in the interferogram j can be written as follows [17,20]:

$$\phi_{ifs_{i,j}} = W\left\{\phi_{def_{i,j}} + \phi_{\mathrm{top}_{i,j}} + \phi_{atm_{i,j}} + \phi_{orbit_{i,j}} + \phi_{noise_{i,j}}\right\} \tag{1}$$

where W stands for wrapping operator; ϕ_{def} is the phase change caused by displacement of the pixel in the satellite line of sight (LOS) direction, ϕ_{top} represents the residual topographic phase error due to inaccuracy of the reference SRTM, ϕ_{atm} accounts for the phase contributed by the difference in atmospheric retardation between interfered image pair, ϕ_{orbit} corresponds to the residual phase due to orbit inaccuracies. The noise term ϕ_{noise} is small enough for a PS point and does not significantly obscure the signal.

The purpose of this study is to achieve an accurate estimation of ϕ_{def}. Thus, the other four terms on the right-hand side of Equation (1) must be estimated and subtracted from the interferometric phase ϕ_{ifs}. Since, the value of ϕ_{ifs} in Equation (1) is a wrapped phase ranging from $-\pi$ to π, a 3-D time-space unwrapping algorithm is adopted to estimate the integer ambiguities of the wrapped phase and finally restore the absolute phase difference of each neighboring PS point [39]. Once the reliable unwrapped phase is available, a least square method is employed to remove the residual topography phase ϕ_{top}, but the remaining phases still contain other disturbances. To achieve better accuracy in estimation of ground deformation, a high-pass temporal filter and a low-pass spatial filter were applied to remove the atmosphere ϕ_{atm} and orbit errors ϕ_{orbit} from the remaining phases, based on the time-space characteristics of these two disturbance terms [20]. We then used the final phase results to calculate the LOS displacement and converted it to the vertical direction to determine the time series deformation. Assuming that the deformation of each point target is $d = [d1,\ d2, \ldots dn]$ and the corresponding time baseline is $T = [T1,\ T2, \ldots Tn]$, then a weighted least square is used to calculate the deformation rate, provided that the mean square error of the interferometric phase serves as the deformation weight.

$$v = \left(T^T P T\right)^{-1} T^T P d \tag{2}$$

where v stands for the deformation velocity, T represents the corresponding time baseline, $d = \frac{\lambda}{4\pi} \cdot \phi_{\mathrm{defo}}$, P is the weight matrix and defined as:

$$P = \mathrm{diag}\left(\sigma^1, \sigma^2, \cdots \sigma^{\mathrm{M}}\right)\ \sigma^k = \sqrt{\frac{\sum_{k=1}^{\mathrm{M}}\left(\hat{\phi}^k_{\mathrm{noise},\ x}\right)^2}{\mathrm{M}} \cdot \frac{180}{\pi}} \tag{3}$$

4. Results and Reliability Analysis

4.1. InSAR-Derived Results

Only a limited number of point targets can be identified using the traditional ADI method. This inevitably has a negative impact on the measurement accuracy of the PSI technique. To expand the application of the PSI technique to reclaimed coastal areas, these low-coherence issues must be resolved as illustrated in Figure 3a.

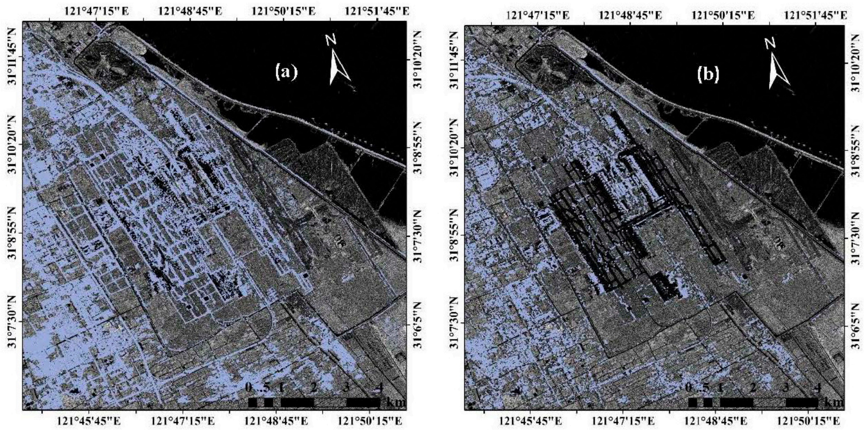

Figure 3. Comparison between the number of selected PS points using the present strategy (**a**) and traditional ADI method (**b**).

Figure 3 shows a comparison of the selected PS points using our proposed strategy and the traditional ADI method. As can be seen, the proposed method has obvious advantages in PS extraction over the traditional method in low-coherence regions. A total of 133,412 points were identified using our strategy (Figure 3a), while only 95,485 points were recognized using the ADI (Figure 3b). More importantly, a large number of point targets lay on the airport runways and taxiways, which made it possible to represent the extent and spatiotemporal behavior of deformation at these runways and taxiways.

Figure 4 shows a map of the ground deformation rate for Pudong Airport obtained using the method described in Section 3. As can be seen, along the airport runways and taxiways, as well as in other low-coherence areas, a large number of dense targets are gathered to represent the deformation behavior features of Pudong Airport. The measured velocity ranges between −3 and +1 cm/year. This image also shows that deformation is concentrated in the runway and peripheral dam areas, while the other areas are almost stable. The airport runway and coastal levee underwent a great deal of deformation during the data acquisition period. Eight areas, represented by points P1–P8 in Figure 4 that fall either on the runways or on the dam, were selected to correlate displacement over time in subsequent analysis. The spatial distribution of the deformation varies with the underlying geological formation conditions and with the cumulative runway operation time, as shown in Figure 4:

1. The first runway has a moderate deformation status with little change in deformation characteristics. The maximum deformation rates in the first runway area was approximately −1.5 cm/year;
2. The second runway shows the most serious deformation among the three runways. Different degrees of uneven deformation rates can be seen in both the north-south profile and east-west profile.
3. The third runway has the most complex difference in deformation rates among the three runways. It has a relatively large deformation gradient in the east-west direction. The displacement in the

P7 area was approximately −0.5 cm/year, while the displacement in the P8 area was more than −2.5 cm/year, a 2.0 cm/year difference.

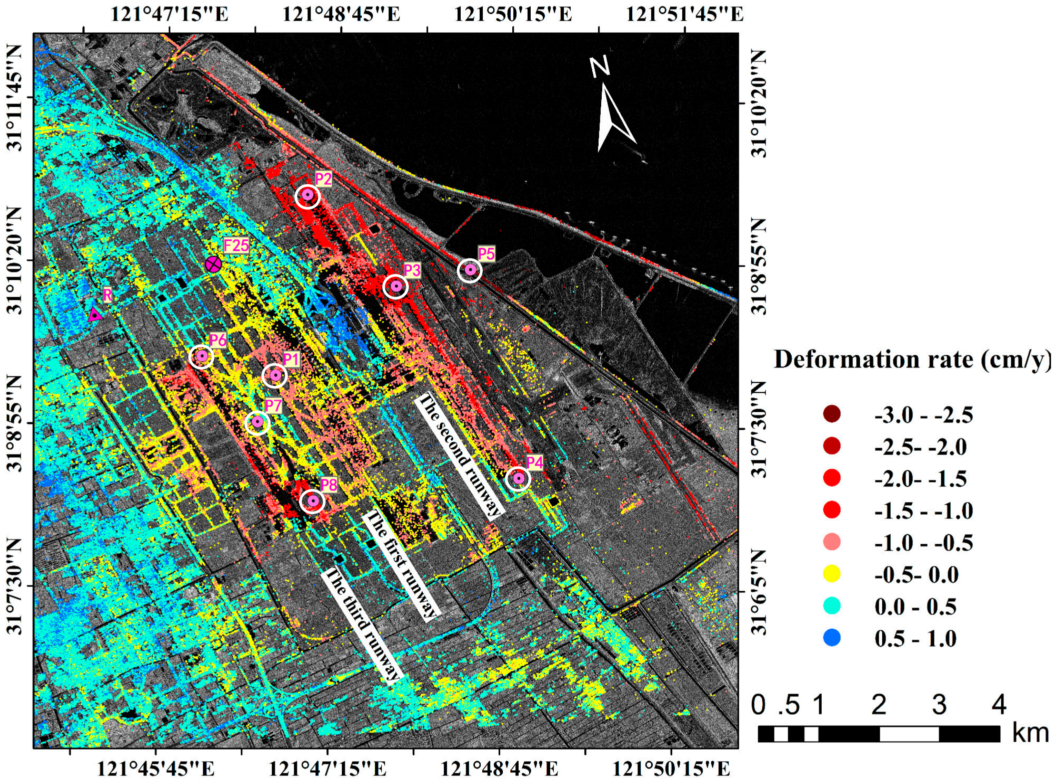

Figure 4. Spatial deformation velocity map of Pudong International Airport.

4.2. Reliability Analysis of the Derived Deformation

The only readily available, independently monitored ground deformation ground-truth point is a time series layerwise mark (F25) located in the north of the study area (Figure 4). During October 2011 and October 2012, the deformation rate at this site was 0.215 cm/year. We observed that the region marked by point R in Figure 4, experienced uplift between September 2011 and October 2012 at a rate of 0.207 cm/year relative to the layerwise mark. Since the observed subsidence is at a regional scale, we used point R as a reference in the following processing [40]. As shown in Figure 4, point R is located in close proximity to the F25 areas; thus, the atmospheric and orbital signals proportional to the distance between the reference point and measurement locations can be ignored.

Figure 5 shows the time series deformation at F25 by layerwise mark leveling and the PSI technique (an average deformation of the total point targets within 20 m around F25). Although the results from the two methods do not strictly align in terms of time, the results are consistent, with a difference of less than 2 mm, confirming the local reliability of InSAR monitoring.

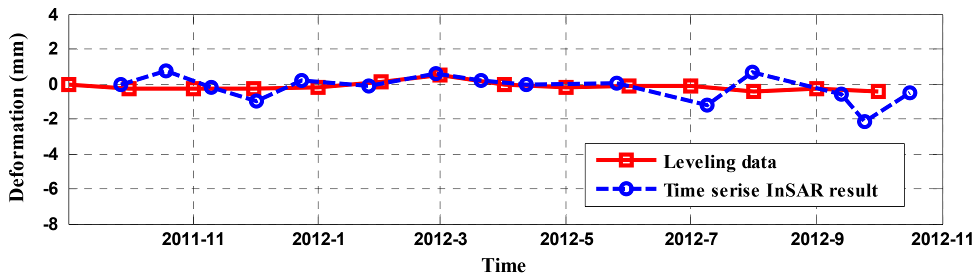

Figure 5. Time series analysis of F25 by layerwise mark leveling and PSI technique.

To illustrate the regional stability of the deformation results, the standard deviation of the mean velocity as derived from the PSI technique was calculated using Formula (4) adopted from [18] and [8]:

$$\sigma_{\Delta v}^2 \approx \left(\frac{\lambda}{4\pi}\right)\frac{\sigma_\varphi^2}{M\sigma_{Bt}^2} \tag{4}$$

where λ is the wavelength of radar-wave, σ_φ represents the phase dispersion, M is the number of interferograms, while σ_{Bt} accounts for the perpendicular baseline deviation of interferograms. As shown in Table 1 presented in Section 2.2, the perpendicular baselines are quite small, which indicate a high accuracy of the deformation velocity. As shown in Figure 6, the standard deviation remained small on each paved runway. The mean standard error of all the target points for the whole area was less than 0.178 cm/year, which implies that the deformation results were stable. This result confirms the reliability of the proposed InSAR technique for deformation detection.

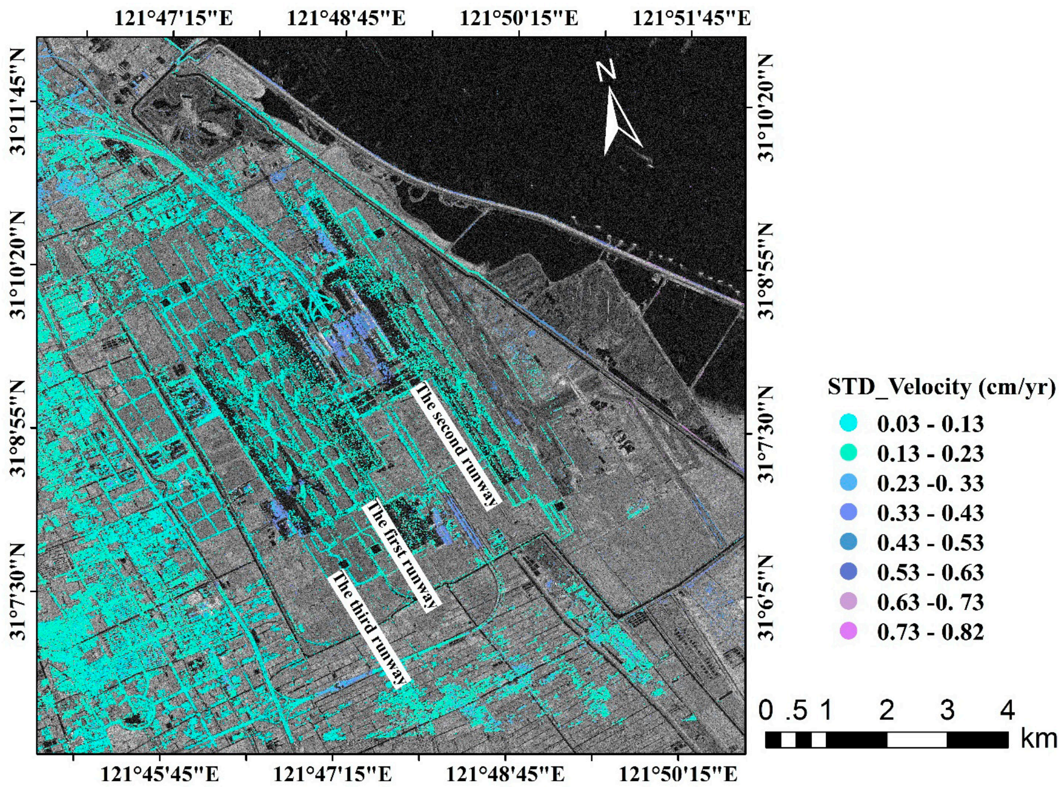

Figure 6. The standard deviation of the mean velocity on coherent point targets.

A statistical analysis of the residual noise was done to estimate the accuracy of the calculated deformation rates. The frequency distribution of the deformation rate shown in the deformation map

(Figure 4) is shown in Figure 7. The deformation rate shown in Figure 4 consists of true ground motion contaminated by residual noise; that is in Figure 7 displayed as a histogram showing more clearly the deformation rates for the PSs.

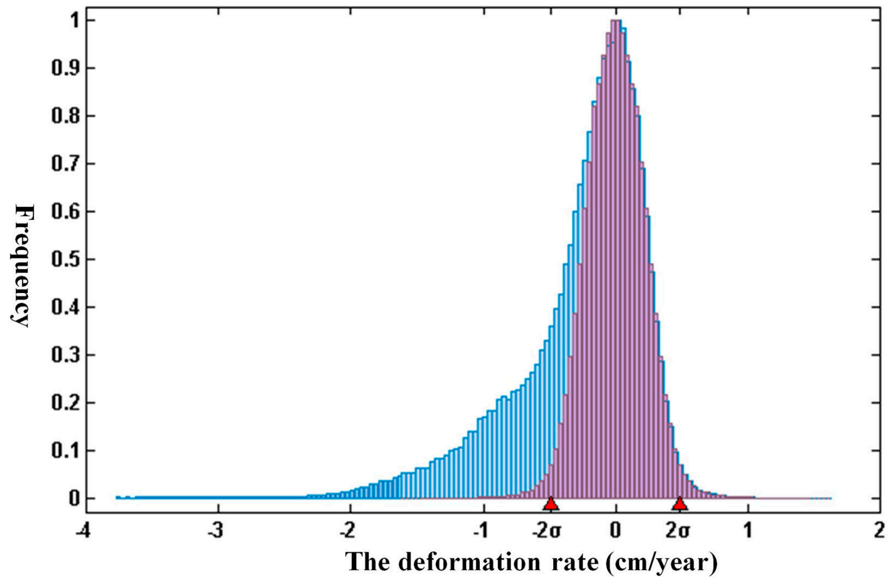

Figure 7. Histogram of vertical deformation rates from Figure 4; red arrows show the 2σ confidence interval.

We assumed that there was no uplift but rather subsidence in the true deformation signal. The deformation rate was calibrated by estimating its mode (approximately equal to zero in this study). The values corresponding to the vertical motion greater than the mode of the distribution were assumed to be noise effects. The other values represent points undergoing true ground motion (the blue colored area seen in Figure 7) and points contaminated by noise. Under the premise that the true noise effect is unknown, the mirrored values of the noise response (values corresponding to the vertical motion greater than the mode) were added. Thus, a nearly Gaussian distribution (purple colored area in Figure 7) was produced, for which we estimated a standard deviation, 0.24 cm/year. The assumption that there was no uplift but subsidence in the study area overestimated the true standard deviation. Based on this calculation, we concluded that the vertical deformation rate with absolute values larger than 2σ = 0.48 cm/year, corresponds to the true ground deformation at a probability of 95% [31,40].

5. Discussion

As described in Section 2.1, the subgrade of Pudong International Airport is built on a soft clay foundation, a weak basic geology with little stability. Foundation settlement is a significant geological problem with safety implications, such as non-uniform settlement of buildings and the adjacent ground. Deformation analysis based on local geological conditions can be crucial to help understand the subsidence mechanism, which could be used for early detection and facilitate preventive diagnosis of potential safety problems in public infrastructure, particularly assisting decision makers in taking mitigation actions to prevent further damages.

5.1. Runways Subgrade

Figure 8 shows a geological section of the runways in regions outside the paleo-river specific area, from 40 m below-ground to several meters above-ground. It can be seen that the spatial distribution of the soil layers and physical mechanics are similar in the mid-range layer groups including ④ mucky clay, and ⑤ clay; and deep range layer groups including ⑦1 sandy silt, and ⑦2 fine-silty sand. Significant differences however, appear in the shallow layer group. In the shallow layer group, ②1 is regarded as a type of crust layer; Layers ②1, ②2, ③1 and ④ are the focus of pre-construction foundation treatments, as they are mainly soft clay, cause settlement, and affect the overall strength of the foundations of buildings and runway structures [41,42].

According to the geological section, the first runway was built on a typical soft soil foundation with complete soil layers from top to bottom [41]. So, the geological section of the first runway was used as a reference for the geological conditions when conducting deformation interpretation. As compared with the foundation of the first runway, the second runway lacks a crust layer ②1, while the third runway was built on shallowly buried mucky silty clay ③1, making the geological foundations of the second and third runways relatively softer and weaker than that of the first runway.

Moreover, the time taken for the land to form for the second runway was the shortest [42]. The region of the second runway did not become beach until the implementation of a reclamation project in the late 1990s. Later, in 2001, the foundation of the second runway was formed by blown sand and backfill, with the addition of partial backfilled fine-silty sand that served as the foundation [41]. Consequently, the condition of the second runway is the weakest and most unstable among the three runways.

According to the runways' geology mentioned above and deformation results plotted in Figure 4, the different geological conditions of runways showed different deformation features:

1. The first runway was put into use in 1999; since then, the subgrade settlement of the runway remained large; subsequently the average cumulative deformation reached 59 cm by 2009. However, during this period, the deformation rate also displayed a slight slowing trend. After more than a decade of consolidation effects of the soft clay, we can infer that the foundation settlement rate should have continuous decreased during the study period [7]. As shown in the deformation result plotted in Figure 4, InSAR results of the ground settlement continued to slow from September 2011 to October 2012, to less than 1.5 cm/year.
2. The second runway, in operation since 2005, lies in the eastern part of the reclaimed land of the airport. The time over which the land formed here was the shortest; the foundation of the second runway was not formed until a 2001 reclamation project [42]. Due to this kind of weak basic geology, the second runway exhibited the most serious deformation, with a maximum deformation rate greater than 2.5 cm/year.
3. The third runway, lying to the west of the first runway, was completed in 2008, with a foundation relatively similar to the first runway. However, since it was completed nine years later than the first runway, the geological base itself still needs further consolidation. Consequently, the third runway underwent more pronounced settlement than the first runway, with a maximum deformation rate greater than 2 cm/year.

This analysis confirmed that the deformation distribution of the runways changes along with the runway subgrades and service time at Pudong International Airport.

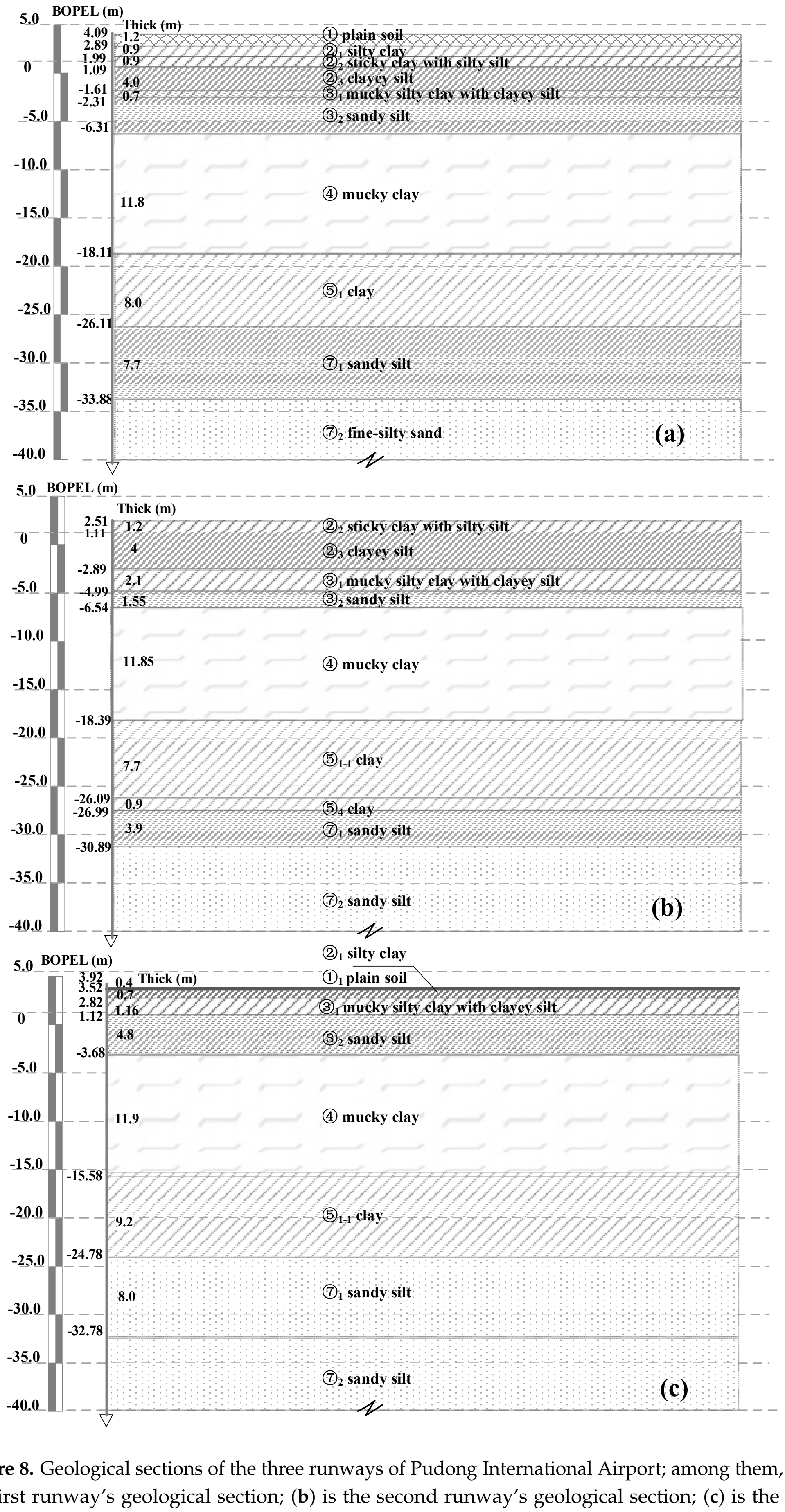

Figure 8. Geological sections of the three runways of Pudong International Airport; among them, (**a**) is the first runway's geological section; (**b**) is the second runway's geological section; (**c**) is the third runway's geological section.

5.2. Geological Environment

In this part, we executed a spatiotemporal analysis in various areas of the airport to study the deformation characteristics and analyze the trigging force. In order to illustrate the temporal evolution of inhomogeneous deformation, we chose eight areas (represented by points P1–P8 in Figures 4 and 9); these areas show relatively large deformation or exhibit large deformation differences compared to their surrounding areas. Subsequently, target points within a 15 m radius of P1–P8 were selected to correlate displacement over time; these target points fall either on the runways or on the dam. As shown in Figure 4, P1 is on the first runway; P2, P3, and P4 are on the second runway; P5 is on the levee; and P6, P7, and P8 are on the third runway. Our further analysis is focused on these subsiding areas.

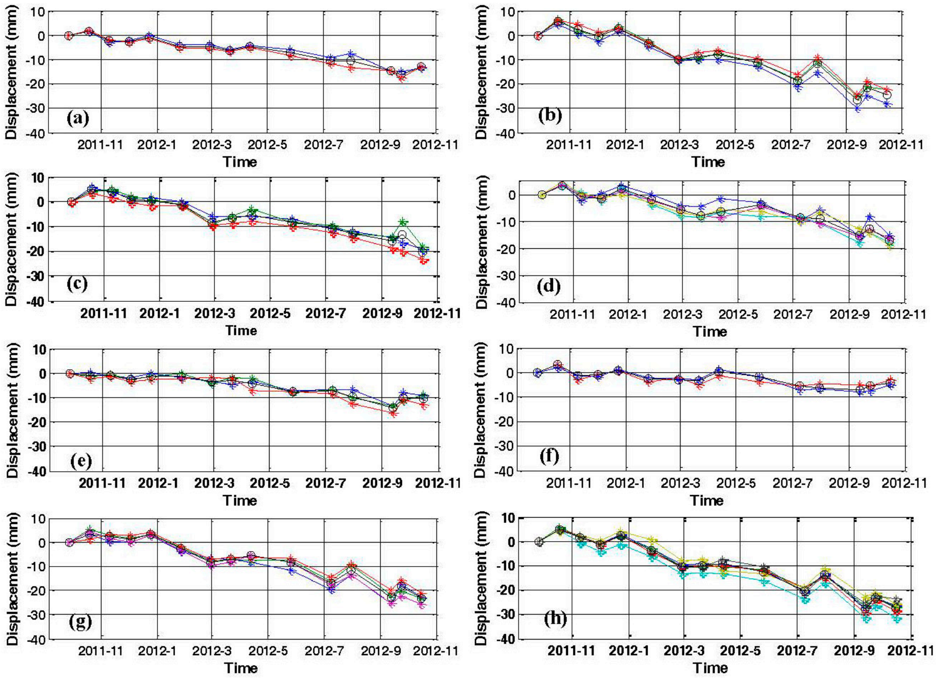

Figure 9. Time series analysis of the selected areas: Deformation of points within a 15 m radius for P1, P2, P3, P4, P6, P7, and P8 are plotted in (**a**–**g**). P5 is plotted separately (**h**).

5.2.1. Paleo-Rivers

Nearby station site and engineering survey data revealed a large-scale paleo-river across the north side of the three runways, from west to east; the thickest deposit layer is approximately 60 m. It is located approximately 940–1420 m from the northern end (P200) of the first runway, with a width that exceeds 500 m. As shown in Figure 1 in the section of study area, another paleo-river crosses the second runway at the south end, with the thickest deposit layer approximately 48 m. The range of coordinates influenced by this second paleo-river ranges from approximately P305 to P320. According to the engineering survey results, the soil around these paleo-rivers is weaker than that in other places. The soil in the bed of the paleo-river is weaker than that on the banks. Therefore, the distribution of the soft soil layer in this area is fairly uneven. Furthermore, many ancient ditches and ponds are scattered throughout this area [43], making the geological environment more complicated.

According to the distribution of paleo-rivers (shown in Figure 1 in section of study area) and the spatial deformation velocity map (Figure 4) as well as the deformation time series analysis of eight selected areas (Figure 9), ground deformation at different positions displays variations related to the variation in soft soil layers. There are different degrees of differential subsidence between paleo-rivers and general areas. For example, near these points, i.e., P1 (marked on the first runway), P3 and P4 (on the second runway), P6 (on the third runway), and P5 (on the dam) found over the paleo-rivers, the deformation values were greater than that found in areas not over the paleo-rivers. Furthermore, due to the silt depth at the mouth of paleo-rivers, the areas adjacent to the sea and close to points P3 and P5 have the largest deformation values among all areas over paleo-rivers, as shown in Figure 9. We conclude from this analysis of the effects of the paleo-rivers that even at the same soil layer, different locations may have different physical and mechanical properties; and, consequently, inhomogeneous deformations often occur when large scale infrastructures, such as airports, are built on land with complex geological histories across many paleo-rivers, ditches or ponds.

5.2.2. Seawater Influence

Whilst, based on an analysis of the regional geological structure, we infer that the closer a foundation is to the sea, the stronger the effects from the sea such as salt water intrusion and flushing corrosion, and thus the foundation is less stable. The flushing corrosion of seawater could lead to foundation rock/soil loose, which reduces the bearing capacity of the foundation and causes foundation settlement, leading to inhomogeneous deformation of infrastructures. While, the salt water intrusion could cause the infiltration of water into soil, resulting in soil compaction, which could also cause ground settlement. As shown in Figure 4, in the second runway area, the deformation of the side adjacent to the sea is larger than the side not adjacent to the sea; the detailed deformation differences can be seen clearly in Figure 9b–d. Moreover, the area of the second runway closest to the sea (i.e., the area around P2) has the most serious deformation in the runway area; the maximum deformation around P2 is approximately 30 mm, as shown in Figure 9b. That is to say, the intrusion and flushing corrosion caused by sea water increases the deformation of structures facing the sea.

5.2.3. Static Load

It is also noteworthy in the Figure 4 that there are large differences in the deformation distribution on the third runway. Since, the main service facility of this third runway system is the freight area on the west side; the foundation of this runway has a permanent static load during the whole period of its operation. Furthermore, at the southern end of the third runway is the air transshipment center of the freight area. The foundation load of the air transshipment center includes static loads from stacked goods and transport equipment as well as loads from moving traffic. Among these loads effects, static load induced displacement (soil consolidation) is the principal type of displacement at the air transshipment center [42]. Hence, static loads are likely the primary factor contributing to the uniform deformation on the third runway visible in Figures 4 and 9e–g.

As can be seen from the analysis in Sections 5.1 and 5.2, the main factors affecting the deformation pattern and gradients at Pudong Airport can be summarized as follows:

1. The geological foundation.
2. Construction time. Under similar geological conditions (e.g., the first and the third runway), the later the time of completion (the third runway), the more serious soil un-compaction and the larger the settlement will be.
3. Paleo-rivers. The soil around the paleo-rivers is weaker than that in other places, thus the paleo-river is an important factor causing inhomogeneous deformation at the airport.
4. Seawater influence. The side of the airport closer to the sea experiences seawater influence, such as salt-water intrusion and flushing corrosion, and thus is weaker than other sides of the airport.
5. Static load. This is likely the primary factor contributing to the uniform deformation pattern found in the third runway area.

5.3. Potential and Notes of InSAR in Monitoring Coastal Subsidence

Our analysis above confirms that the deformation results using the proposed PSI technique harmonize with the regional geological environmental conditions. In order to properly map the coastal deformation induced by land reclamation, the low-coherence effect must be settled during the data processing. To illustrate this problem, a comparison of the identified PS points using a traditional ADI method and the proposed strategy were given in Figure 3, Section 3.2. Results showed that few PS have been selected by ADI in the areas of airport runways and taxiways. While our method has much denser PS points in the whole airport region, especially along the runways and taxiways, which made it possible to represent the extent and spatiotemporal behavior of deformation in these low-coherence areas. Thus, the modified method has great potential in coastal deformation detection and monitoring. However, the proposed method also has its limitations. First, the value of each threshold for PS selection needs to be carefully determined during the iterative process. Second, the deformation measurements in this study are under the assumption of non-horizontal displacement. Thus, only vertical displacement is obtained. Whereas, the horizontal displacement cannot always be ignored especially when large subsidence occurs. Therefore, joint analyses of ascending and descending datasets or different viewing angles datasets can be considered for 3D displacement inversion later.

It is worth remarking that not all coastal zones present subsidence signals reflecting the geological environment in the deformation measurements. Take Terminal II, (between the first and second runway) for example, it was in an uplifted state during the InSAR monitoring period. We believe this uplifted state occurred for the following reasons. The first is topographic error. Terminal II is a complex structure with a wave-like curve design, and it is easy to misestimate the topographic error [44]. For this type of building, a high-precision, three-dimensional digital terrain map must be employed to decrease the terrain error effectively. The second reason is deformation induced by temperature differences. Since Terminal II is constructed of glass, steel, and concrete, the glazing curtain wall, steel plate roofing, and large horizontally placed skylights make Terminal II a large heat transfer area that is easily affected by temperature variations [45]. To avoid error induced by these temperature variations, synchronous temperature measurements of the structure are needed to help select interferograms with small temperature differences for subsequent deformation calculations.

6. Conclusions

To meet the growing demand for land for urban construction and transportation, a site with 40 km^2 of coastal land has been reclaimed from the sea for the construction of Shanghai Pudong International Airport. However, the foundations of reclaimed land are susceptible to settlement and could have undesirable environmental impacts that could adversely affect these dense, populated areas. At present, there are approximately 130,000 passengers arriving or departing from this airport every day; thus, the stability of the airport subgrade is of public concern.

In this present study, an analysis of spatial and temporal behavior of deformation at Shanghai Pudong International Airport was carried out by applying a modified PSI method to high resolution TerraSAR-X satellite image stack, collected for the period 2011 to 2012. A point selection strategy that unites the Amplitude Dispersion Index (ADI) with a coherence-like coefficient was applied for PS point recognition in low-coherence areas. A total of 132,126 points with a density of approximately 500/km^2 were identified in the study area. Based on this, the spatiotemporal behavior of deformation at the airport, including the runways and taxiways, was depicted in detail. To evaluate the stability and confidence of the monitoring results, a statistical analysis were implemented, showing that the deformation rate with absolute values larger than $2\sigma = 0.48$ cm/year corresponds to the true ground deformation at a 95% probability.

Since, the subgrade of the Pudong area is built on a soft clay foundation, the complex underlying geological conditions and building foundation types, in addition to ongoing construction activities, make it difficult to interpret InSAR-derived results. Our interpretations and analysis of the deformation results were conducted with local geological data and reclamation evolution information available. The qualitative spatiotemporal analysis of the deformation verified that the variation trends in the InSAR monitoring results coincide with the change in the geological environment. The factors responsible for the deformation in the airport region were analyzed and summarized to help understand the deformation mechanisms. These results demonstrate that our proposed approach has great potential for deformation monitoring of transportation facilities built in low-coherence regions, like the ocean reclaimed land; and could facilitate preventive diagnosis of potential safety problems in public infrastructure, thus assisting decision makers and planners in ensuring safe operations and sustainability.

Acknowledgments: This work is financially supported by the National Natural Science Foundation of China (Grant No. 61331016, No. 41571435 and No. 41521002) and the Open Fund of State Key Laboratory of Geohazard Prevention and Geoenviroment Protection (Grant No. SKLGP2017K016). The authors would like to thank the Astrium Satellite Company and the German Aerospace Center (DLR) for providing the TerraSAR-X datasets and the Shanghai Institute of Geological Survey for providing time series layerwise mark data.

Author Contributions: Y.J. implemented the methodology and finished the manuscript organization. M.L. and L.Z. supervised the research and provided valuable suggestions for the revision. H.W. made contributions to interpreting the InSAR-derived results within a geologic setting, T.B. did a lot of work on language revisions to make the manuscript read well in English. All authors have read and approved the final manuscript and agreed to be listed.

Conflicts of Interest: The authors declare no conflict of interest.

References

1. Glaser, R.; Haberzettl, P.; Walsh, R. Land reclamation in Singapore, Hong Kong and Macau. *GeoJ* **1991**, *24*, 365–373. [CrossRef]
2. Stuyfzand, P.J. The impact of land reclamation on groundwater quality and future drinking water supply in the Netherlands. *Water Sci. Technol.* **1995**, *31*, 47–57. [CrossRef]
3. Kim, S.W.; Lee, C.W.; Song, K.Y.; Min, K.; Won, J.S. Application of L-band differential SAR interferometry to subsidence rate estimation in reclaimed coastal land. *Int. J. Remote Sens.* **2005**, *26*, 1363–1381. [CrossRef]
4. Hoeksema, R.J. Three stages in the history of land reclamation in the Netherlands. *Irrig. Drain.* **2007**, *56*, S113–S126. [CrossRef]
5. Pickles, A.; Tosen, R. Settlement of reclaimed land for the new Hong Kong international airport. *ICE Proc. Geotech. Eng.* **1998**, *131*, 191–209. [CrossRef]
6. Douglas, I.; Lawson, N. Airport construction: Materials use and geomorphic change. *J. Air Transp. Manag.* **2003**, *9*, 177–185. [CrossRef]
7. Jiang, L.; Lin, H. Integrated analysis of SAR interferometric and geological data for investigating long-term reclamation settlement of Chek Lap Kok airport, Hong Kong. *Eng. Geol.* **2010**, *110*, 77–92. [CrossRef]
8. Wang, T.; Perissin, D.; Rocca, F.; Liao, M.S. Three Gorges Dam stability monitoring with time-series InSAR image analysis. *Sci. China Earth Sci.* **2011**, *54*, 720–732. [CrossRef]
9. Gabriel, A.K.; Goldstein, R.M.; Zebker, H.A. Mapping small elevation changes over large areas: differential radar interferometry. *J. Geophys. Res. Solid Earth* **1989**, *94*, 9183–9191. [CrossRef]
10. Hanssen, R.F. *Radar Interferometry: Data Interpretation and Error Analysis*; Springer Science & Business Media: Berlin, Germany, 2001; Volume 2.
11. Ding, X.; Liu, G.; Li, Z.W.; Li, Z.L.; Chen, Y.Q. Ground subsidence monitoring in Hong Kong with satellite SAR interferometry. *Photogramm. Eng. Remote Sens.* **2004**, *70*, 1151–1156. [CrossRef]
12. Wang, Y.; Liao, M.S.; Li, D.R.; Wei, Z.X.; Fang, Z. Subsidence velocity retrieval from long-term coherent targets in radar interferometric stacks. *Chin. J. Geophs. Chin. Ed.* **2007**, *50*, 598–604.
13. Jiang, M.; Li, Z.W.; Ding, X.L.; Zhu, J.J.; Feng, G.C. Modeling minimum and maximum detectable deformation gradients of interferometric SAR measurements. *Int. J. Appl. Earth Obs.* **2011**, *13*, 766–777. [CrossRef]
14. Tomás, R.; Romero, R.; Mulas, J.; Marturià, J.J.; Mallorquí, J.J.; López-Sánchez, J.M.; Herrera, G.; Gutiérrez, F.; González, P.J.; Fernández, J. Radar interferometry techniques for the study of ground subsidence phenomena: A review of practical issues through cases in Spain. *Environ. Earth Sci.* **2014**, *71*, 163–181. [CrossRef]
15. Dong, S.; Samsonov, S.; Yin, H.; Yao, S.; Xu, C. Spatio-temporal analysis of ground subsidence due to underground coal mining in Huainan coalfield, China. *Environ. Earth Sci.* **2015**, *73*, 5523–5534. [CrossRef]
16. Massonnet, D.; Feigl, K.L. Radar interferometry and its application to changes in the earth's surface. *Rev. Geophys.* **1998**, *36*, 441–500. [CrossRef]

17. Ferretti, A.; Prati, C.; Rocca, F. Permanent scatterers in SAR interferometry. *IEEE Trans. Geosci. Remote Sens.* **2001**, *39*, 8–20. [CrossRef]
18. Colesanti, C.; Ferretti, A.; Novali, F.; Prati, C.; Rocca, F. SAR monitoring of progressive and seasonal ground deformation using the Permanent Scatterers Technique. *IEEE Trans. Geosci. Remote Sens.* **2003**, *41*, 1685–1701. [CrossRef]
19. Lyons, S.; Sandwell, D. Fault creep along the southern San Andreas from interferometric synthetic aperture radar, permanent scatterers, and stacking. *J. Geophys. Res. Solid Earth* **2003**, *108*. [CrossRef]
20. Hooper, A.J. Persistent scatter radar interferometry for crustal deformation studies and modeling of volcanic deformation. Ph.D. Thesis, Stanford University, Stanford, CA, USA, 2006.
21. Kampes, B.M. *Radar Interferometry: Persistent Scatterer Technique*; Springer: Dordrecht, The Netherlands, 2006.
22. Sousa, J.J.; Ruiz, A.M.; Hanssen, R.F.; Bastos, L.; Gil, A.J.; Galindo-Zaldívar, J.; de Galdeano, C.S. PS-InSAR processing methodologies in the detection of field surface deformation—Study of the Granada Basin (Central Betic Cordilleras, southern Spain). *J. Geodyn.* **2010**, *49*, 181–189. [CrossRef]
23. Pei, Y.; Liao, M.; Wang, H. Monitoring subsidence in reclamation area with time series DInSAR images. *Geomat. Inf. Sci. Wuhan Univ.* **2012**, *37*, 1092–1095.
24. Jendryke, M.; Balz, T.; Jiang, H.; Liao, M.; Stilla, U. Using open-source components to process interferometric TerraSAR-X spotlight data. *Int. J. Antennas Propag.* **2013**, *2013*, 275635. [CrossRef]
25. Hooper, A.; Zebker, H.; Segall, P.; Kampes, B. A new method for measuring deformation on volcanoes and other natural terrains using InSAR persistent scatterers. *Geophys. Res. Lett.* **2004**, *31*, 1–5. [CrossRef]
26. Ferretti, A.; Savio, G.; Barzaghi, R.; Borghi, A.; Musazzi, S.; Novali, F.; Prati, C.; Rocca, F. Submillimeter accuracy of InSAR time series: Experimental validation. *IEEE Trans. Geosci. Remote Sens.* **2007**, *45*, 1142–1153. [CrossRef]
27. Osmanoğlu, B.; Dixon, T.H.; Wdowinski, S.; Cabral-Cano, E.; Jiang, Y. Mexico city subsidence observed with persistent scatterer InSAR. *Int. J. Appl. Earth Obs.* **2011**, *13*, 1–12. [CrossRef]
28. Abdikan, S.; Arıkan, M.; Sanli, F.B.; Cakir, Z. Monitoring of coal mining subsidence in peri-urban area of Zonguldak city (NW Turkey) with persistent scatterer interferometry using ALOS-PALSAR. *Environ. Earth Sci.* **2014**, *71*, 4081–4089. [CrossRef]
29. Perissin, D.; Wang, Z.; Lin, H. Shanghai subway tunnels and highways monitoring through Cosmo-SkyMed Persistent Scatterers. *ISPRS J. Photogramm.* **2012**, *73*, 58–67. [CrossRef]
30. Wu, J.; Zhang, L.; Chen, J.; Li, T. Monitoring ground subsidence in shanghai maglev area using two kinds of SAR data. *J. Appl. Geod.* **2012**, *6*, 209–213. [CrossRef]
31. Dong, S.C.; Samsonov, S.; Yin, H.W.; Ye, S.J.; Cao, Y.R. Time-series analysis of subsidence associated with rapid urbanization in Shanghai, China measured with SBAS InSAR method. *Environ. Earth Sci.* **2014**, *72*, 677–691. [CrossRef]
32. Zhao, Q.; Pepe, A.; Gao, W.; Lu, Z.; Bonano, M.; He, M.L.; Wang, J.; Tang, X. A DInSAR investigation of the ground settlement time evolution of ocean-reclaimed lands in Shanghai. *IEEE J. Sel. Top. Appl. Earth Obs. Remote Sens.* **2015**, *8*, 1673–1781. [CrossRef]
33. Jiang, L.; Lin, H.; Cheng, S. Monitoring and assessing reclamation settlement in coastal areas with advanced InSAR techniques: Macao city (China) case study. *Int. J. Remote Sens.* **2011**, *32*, 3565–3588. [CrossRef]
34. Zhao, Q.; Lin, H.; Gao, W.; Zebker, H.A.; Chen, A.; Yeung, K. InSAR detection of residual settlement of an ocean reclamation engineering project: A case study of Hong Kong international airport. *J. Oceanogr.* **2011**, *67*, 415–426. [CrossRef]
35. Baeteman, C. Vulnerability of coastal lowlands. A case study of land subsidence in Shanghai, P.R. China. In *Greenhouse Effect, Sea Level and Drought*; Paepe, R., Fairbridge, R.W., Jelgersma, S., Eds.; Springer: Dordrecht, The Netherlands, 1990; pp. 415–426.
36. Gong, S. Effects of urban construction on the land subsidence in Shanghai. *Chin. J. Geol. Hazard Control* **1998**, *9*, 108–111.
37. U.S. Geological Survey. USGS EarthExplorer. Available online: https://earthexplorer.usgs.gov/ (accessed on 9 December 2016).
38. Zebker, H.; Chen, K. Accurate estimation of correlation in InSAR observations. *IEEE Lett. Geosci. Remote Sens.* **2005**, *2*, 124–127. [CrossRef]
39. Hooper, A. A Statistical-Cost Approach To Unwrapping The Phase Of InSAR Time Series. In Proceedings of the International Workshop on ERS SAR Interferometry, Frascati, Italy, 30 November–4 December 2009.

40. Samsonov, S.V.; d'Oreye, N.; González, P.J.; Tiampo, K.F.; Ertolahti, L.; Clague, J.J. Rapidly accelerating subsidence in the greater vancouver region from two decades of ERS-ENVISAT-RADARSET-2 DInSAR measurements. *Remote Sens. Environ.* **2014**, *143*, 180–191. [CrossRef]
41. Wang, X.H.; Yin, C.L.; Si, B.F.; Li, J.S.; Liu, S.; Su, E.H. Foundation bed treatment for high-grade taking-off and landing runway-study on construction proposal for the third runway of Shanghai Pudong international airport building construction. *Build. Constr.* **2007**, *29*, 275–277.
42. Wang, G.D.; Han, L.M.; Chai, Z.L. Subgrade settlement rules of first runway of Pudong airport in Shanghai. *J. Eng. Geol.* **2012**, *20*, 131–137.
43. Wang, Z. *A Combined Reinforcement Method for Shallow Soft Soil Foundation*; Shanghai Scientific and Technical Publishers: Shanghai, China, 2006.
44. Slatton, K.C.; Crawford, M.M.; Gibeaut, J.C.; Gutierrez, R. Removal of residual errors from SAR -derived digital elevation models for improved topographic mapping of low-relief areas. In Proceedings of International Geoscience and Remote Sensing Symposium on Remote Sensing: A Scientific Vision for Sustainable Development, Singapore, 3–8 August 1997; pp. 457–459.
45. Crosetto, M.; Monserrat, O.; Cuevas-Gonzaìlez, M.; Devantheìry, N.; Crippa, B. Analysis of X-band very high resolution persistent scatterer interferometry data over urban area. In Proceedings of the International Archives of the Photogrammetry, Remote Sensing and Spatial Information Science, Hannover, Germany, 1–24 May 2013; pp. 21–24.